Terahertz metamaterial absorber based on single pattern pentagon shaped resonator for high Q sensing

A. ELAKKIYA*
Saveeetha Engineering College, Saveetha Nagar, Chennai, 602 105, India

A novel terahertz (THz) Metamaterial Absorber (MMA) is presented in this paper. It consists of a pentagon shaped resonator as a unit cell and a copper as ground plane which are separated by a 0.125 mm polyimide dielectric substrate. Unlike conventional absorbers that have single-functional absorption behavior of broadband or multi-band, the proposed device exhibits both, thirteen-band and nine-band. This is achieved by adjusting the single top patch geometrical parameter. The designed structure enables thirteen absorption peaks, of which the first, tenth and thirteenth peaks have 99% absorptivity while the sixth peak possesses a high quality factor (*Q*) value of 423. Moreover, the figure of merit (FOM) of the sixth absorption peak can reach 50, which is much higher than that of the other absorption modes. The proposed structure is working well for wide incident angles and polarization angles wave up to 90^0. The physical mechanism of the structure is analyzed by electric and magnetic field distributions. We compared the resonant frequency ranges and number of bands in this work with previous reported papers. The unique feature of the design is that it offers both polarization-sensitive-/insensitive and angle-insensitive-/sensitive absorption characteristics depending on the frequency of operation. In terahertz range, this is the first time a single planar structure provides thirteen and nine-band high-level absorption performances with sensing.

(Received November 1, 2021; accepted June 7, 2022)

Keywords: Thirteen-/nine-band MMA, Polarization and incident angle sensitive-/insensitive, Terahertz

1. Introduction

Many researchers placed the basics for ground-breaking the field of electromagnetic (EM) in the second half of the 20th century. If the materials have negative permittivity and negative permeability, these materials are called the metamaterials (MM) or artificial materials have a numerous applications ranging from microwave to optical frequencies. They can achieve unusual EM properties that are not available in nature, such as negative index of refraction, perfect lensing and cloaking [1-6]. Based on these properties many number of devices have been proposed, such as antennas, filters, solar cells, switches, sensors, and modulators [7-12]. In realistic applications, the absorption losses are unavoidable in metamaterials, which frequently decreases their performance. Therefore, considerable attentions have been rewarded to make devices with a low-loss. Some structures are obtainable to reduce the absorption losses through particular methods, for example by gain materials and by using optimizing structural geometries. However, the intrinsic losses of the MM are helpful for an artificial light absorber. Furthermore, not only could it be improved extremely but also it can attain perfect absorption by designing a proper MMA structure. These multiband absorbers will be used in sensing, imaging, solar cells, photo detectors, cloaking applications, filters and thermal emitters [13].

As is famous, the first MMA is offered by Landy et al. in 2008, which consists of a split-ring-resonator (SRR) and a metallic cut-wire estranged by a substrate with the absorption rate of 88%. In effect, the structure of MMAs is one type of lossy high impedance plane that proved to have the capacity to absorb [14]. Initially, single-band MMAs were designed but consequently, researchers tried to increase the number of bands. Octa-band [15], hepta-band [16], hexa-band [17], penta-band [18], quad-band [19], triple-band [20], dual-band [21] and narrow band [22] absorption characteristics were obtained in the terahertz area. Several of these are difficult as they wanted multi-layered structures and multiple resonators into a single unit-cell. So, simple designs that are able of producing multi-band characteristics are being favored in the recent years [23-25]. It can be done that none of the designed MMAs are capable of showing more than eight absorption bands. In this paper, we proposed a novel multi-band MMA which consists of a single pentagon shaped resonator. The thirteen-bands are obtained at 0.77 THz, 0.78 THz, 0.8 THz, 0.81 THz, 0.84 THz, 0.85 THz, 0.86 THz, 0.87 THz, 0.876 THz, 0.88 THz, 0.89 THz, 0.9 THz and 0.94 THz with the absorption rate of 99.8 %, 93 %, 96 %, 78%, 90 %, 87 %, 94 %, 86 %, 95 %, 99.9 %, 84 %, 97 % and 99 % respectively. The nine-bands are obtained at 0.78 THz, 0.79 THz, 0.82 THz, 0.83 THz, 0.85 THz, 0.86 THz, 0.89 THz, 0.92 THz and 0.93 THz with the absorption rate of 97 %, 93 %, 99%, 99%, 92%, 94 %, 99.9 %, 82 % and 88 % respectively. The highlights of our proposed terahertz MMA structure in comparison with previous THz MMs are, this has a very simple unit-cell structure and high resonant modes mechanism within short frequency range of 0.76 - 0.96 THz without the stacked layers; this MMA can provide thirteen-/nine-band high-level absorption performance in a single planar structure for the first time in terahertz range;

Another unique feature of the design is that it offers both polarization-sensitive-/insensitive and angle-insensitive-/sensitive absorption characteristics depending on the frequency of operation, when the angle of polarization and incidence of the electromagnetic wave is varied. Particularly, the design gives a significant ability to shift the resonance frequencies by changing different geometric parameters. The sixth peak possesses a high *Q* value of 423 and corresponding FOM of the absorption peak can reach 50.

2. Structure and design

The proposed thirteen-/nine-band terahertz MMA structure is shown in Fig. 1(a) and periodic view of MMA is shown in Fig. 1(b). The top and the bottom metal layer are separated by polyimide dielectric substrate. The MMA structure consists of pentagon shaped resonator made up of copper that are merged together and have a thickness of 0.001 mm. The ground plane is entirely made of copper and has a thickness of 0.001 mm with a frequency-insensitive conductivity of $\sigma=5.8\times10^7$ S/m. Polyimide has a thickness of 0.125 mm.

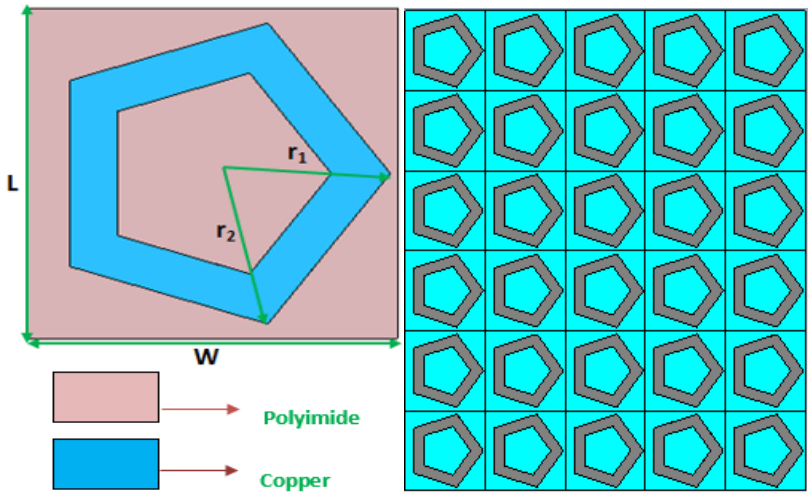

(a) *(b)*

Fig.1(a). Unit cell of the proposed Terahertz MMA, (b) Periodic view of the Terahertz MMA (color online)

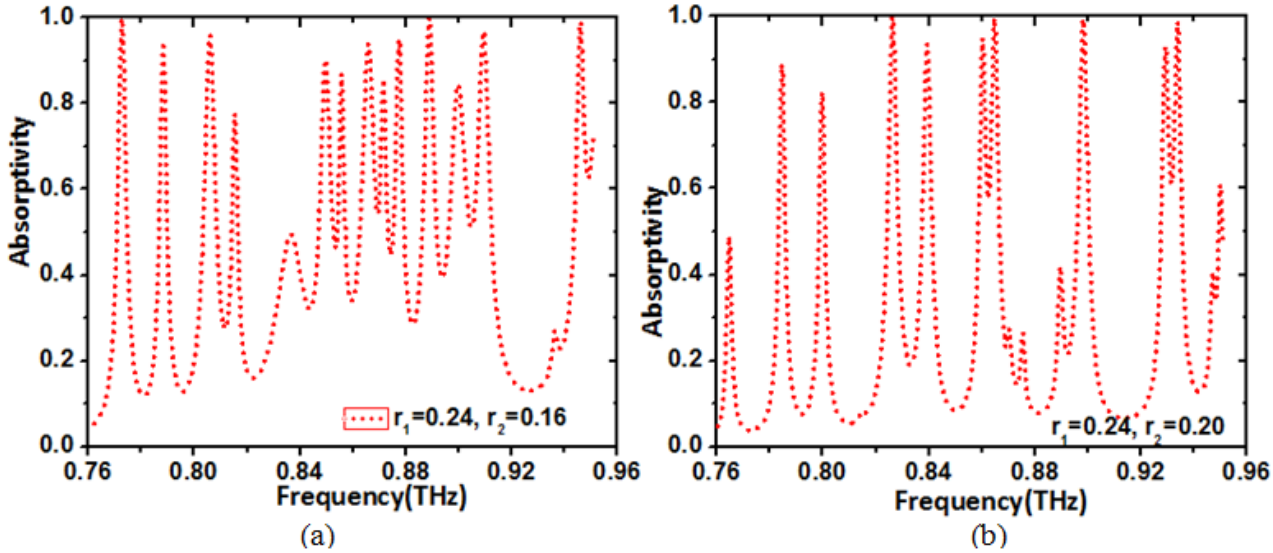

Fig. 2. Absorption curves for (a) thirteen-band, (b) nine-band MMA (color online)

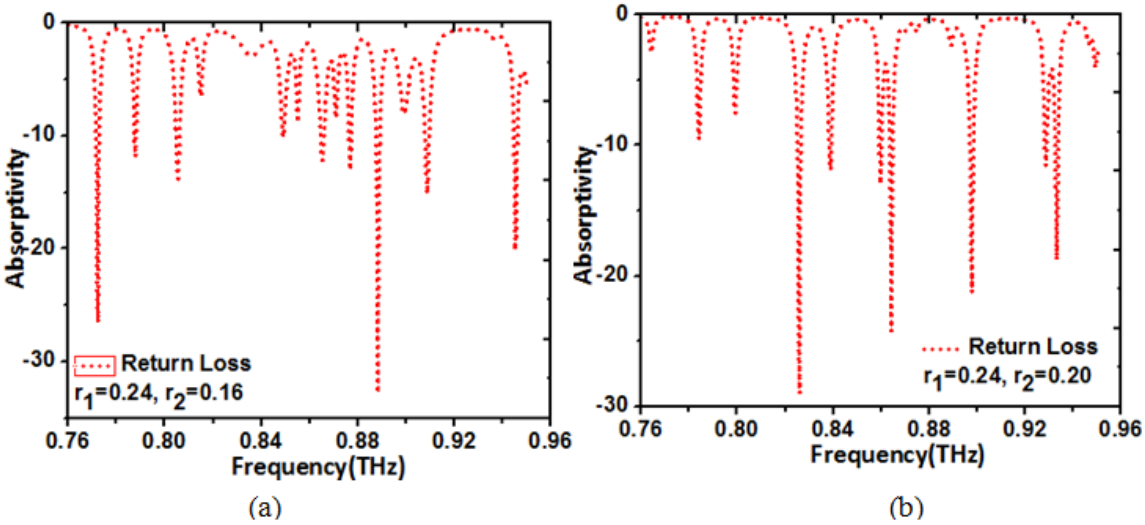

Fig. 3. Return loss for (a) thirteen-band, (b) nine-band MMA (color online)

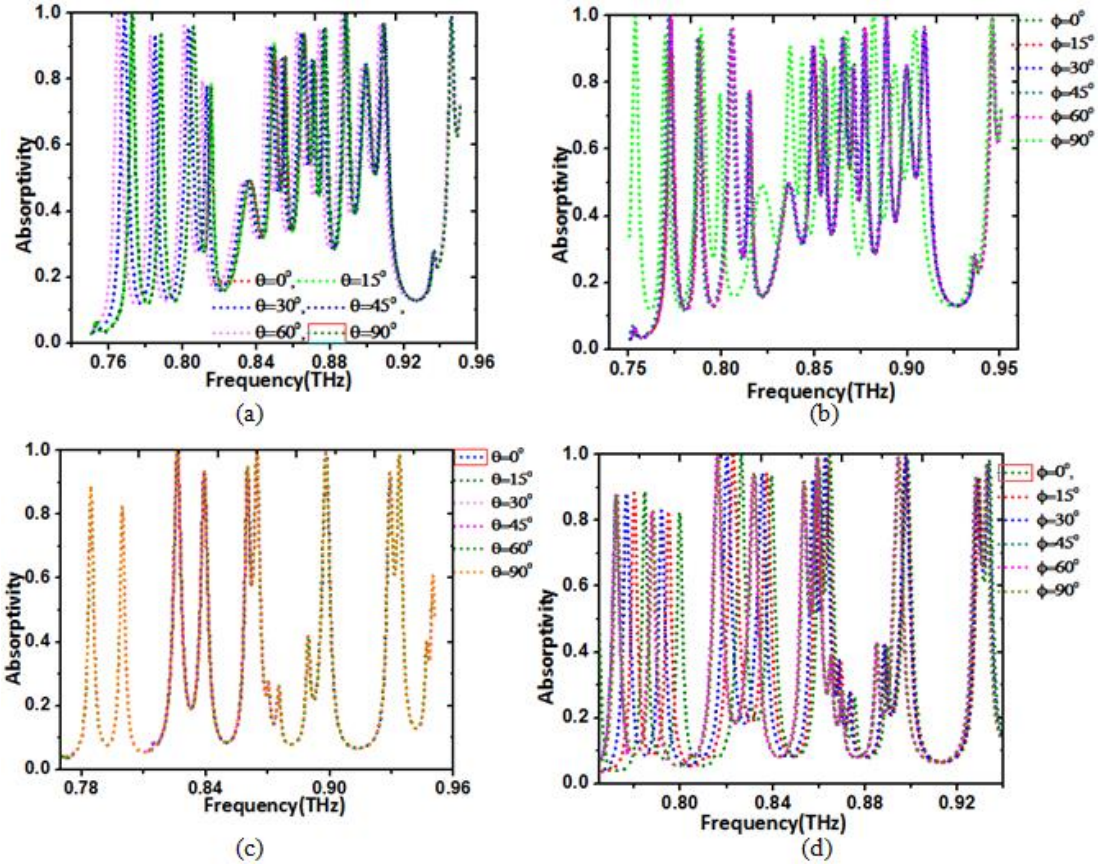

Fig. 4. Absorption characteristics of the thirteen-/nine-band absorber (a)(c) different oblique angle incidence (b)(d) different polarization angles (color online)

Its dielectric constant (ε_r) value is 3.5 and electric tangent (tan δ) value is 0.0027. The other dimensions of the structure are outer radius r_1=0.24, inner radius r_2=0.16 (for thirteen-band), 0.2 (nine-band). The size (width = 0.5 mm, length = 0.5 mm) of dielectric substrate and metallic bottom ground plane are the same. The absorption behavior, structure efficiency and sensing are demonstrated by using commercially available Computer Simulation Technology (CST) microwave studio software. For the simulations, periodic boundary conditions were used for a unit cell in *x* and *y* directions and *z* plane has a perfectly matched open layer boundary condition. The absorption is calculated by A (ω) = 1 - R (ω) - T (ω), Where R (ω) is reflection and T (ω) is transmission. Since the thickness of the ground metal layer is larger than its skin depth, T (ω) goes to zero. Therefore, A (ω) goes to one. The mesh configuration is

very important to get the good results. The mesh notion is a main factor to the time domain solver. The mesh type and size are often specified automatically and precisely by CST in the frequency domain solver, resulting in improved accuracy.

3. Results and discussions

3.1. Absorption characteristics

The design simulation of the proposed structure is carried out using Computer Simulation Tool microwave studio software. The simulated absorbance of the proposed terahertz thirteen-/nine-band MMA is presented in Fig. 2 (a) (b). The absorber is resonated at thirteen frequencies 0.77 THz, 0.78 THz, 0.8 THz, 0.81 THz, 0.84 THz, 0.85 THz, 0.86 THz, 0.87 THz, 0.876 THz, 0.88 THz, 0.89 THz, 0.9 THz and 0.94 THz with the absorption rate of 99.8 %, 93 %, 96 %, 78%, 90 %, 87 %, 94 %,

86 %, 95 %, 99.9 %, 84 %, 97 % and 99 % respectively. When the inner radius of the pentagon shaped resonator is varied from 0.16 mm to 0.2 mm the same structure resonated at nine different frequencies 0.78 THz, 0.79 THz, 0.82 THz, 0.83 THz, 0.85 THz, 0.86 THz, 0.89 THz, 0.92 THz and 0.93 THz with the absorption rate of 97 %, 93 %, 99%, 99%, 92%, 94 %, 99.9 %, 82 % and 88 % respectively. The return loss characteristics for both thirteen-/nine-band MMA are presented in Fig.3 (a) (b). Polyimide based absorber structure gives return loss below -10 dB; hence it is used to achieve the near-unity absorption. The important characteristic of an absorber is its capability to absorb EM spectrum incident on its surface over polarization angle and incident angle. The effect of incidence angle on the thirteen-band absorption spectra is analyzed and the results are shown in Fig. 4 (a). It can be observed that the absorption spectra at 0.89 THz, 0.9 THz and 0.94 THz remain almost unchanged with the variation in incident angles. Especially, the 0.94 THz absorption band is extremely significant because of its high absorption (almost 99 % at normal incidence) and has tremendous applications due to the absorber's insensitivity to variations in incidence angle at this frequency. The absorption spectra at 0.77 THz, 0.78 THz, 0.8 THz and 0.81 THz is found to slightly shift towards lower frequencies with the increase in incidence, but there is also maintain the amount of absorption offered by the structure. The absorption band at 0.84 THz, 0.85 THz, 0.86 THz, 0.87 THz, 0.876 THz and 0.88 THz was almost unchanged except for a slight shift towards lower frequencies with the increase in incidence. Thus, the structure offers angle-insensitive and angle-sensitive absorption spectra based on the frequency of operation. The effect of the polarization angle on the thirteen-band absorption spectra is analyzed and the results are shown in Fig. 4 (b). It can be observed that the absorption spectra of the structure are polarization insensitive up to 60^0. For 90^0 the absorption curves are shifted to the lower frequency side except 0.94 THz. Thus, the structure offers polarization-insensitive and polarization -sensitive absorption spectra based on the frequency of operation.

The effect of incidence angle on the nine-band absorption spectra is analyzed and the results are shown in Fig. 4 (c). The oblique incident angle is varied from 0 to 90^0 for the whole frequency range (0.76 to 0.96 THz) of interest. Absorption and a resonant frequency of the structure did not vary while changing the incident angle values. Therefore, the proposed MMA exhibits an excellent angle independent absorption performance. This is mainly due to the unit cell structure of the designed MMA. The effect of the polarization angle on the nine-band absorption spectra is analyzed and the results are shown in Fig. 4 (d). It can be observed that the absorption spectra at 0.92 THz and 0.93 THz remain almost unchanged with the variation in polarization angles. The absorption spectra at 0.78 THz, 0.79 THz, 0.82 THz, 0.83 THz, 0.85 THz, 0.86 THz and 0.89 THz is found to slightly shift towards lower frequencies with the increase in polarization angle, but there is also maintain the amount of absorption offered by the structure. Thus, the structure offers polarization-insensitive and polarization -sensitive absorption spectra based on the frequency of operation.

3.2. Electric field distributions (E - field)

The method behind the absorption mechanism can be further explained with the help of the electric and magnetic field distribution diagrams. The electric field distribution diagram for these thirteen absorption bands is shown in Fig. 5. It can be observed from Fig. 5 (a), (b) that the absorption mode at 0.77 THz, 0.78 THz respectively, is obtained due to the field distribution near the bends of the resonator, which is caused by the slowing of charges near the bends and on the surface of the dielectric. For the frequency of 0.8 THz and 0.81 THz the E-field is maximum at the surface of the dielectric and the outer edges, bends of the pentagon resonator. For the frequency of 0.84 THz, 0.85 THz, 0.86 THz and 0.87 THz the E-field is maximum at the surface of the dielectric and the inner and outer edges, bends of the pentagon resonator. When the frequency is 0.876 THz the E-field is maximum at whole patch structure and some places in surface of the dielectric. For the frequency of 0.88 THz, 0.89 THz, 0.9 THz and 0.94 THz the E-field is maximum at the inner and outer edges, bends of the pentagon resonator and the surface of the dielectric.

The electric field distribution diagram for nine absorption bands is shown in Fig. 6. When the frequency is 0.78 THz the E-field is maximum at patch structure and some places in surface of the dielectric. For the frequency of 0.79

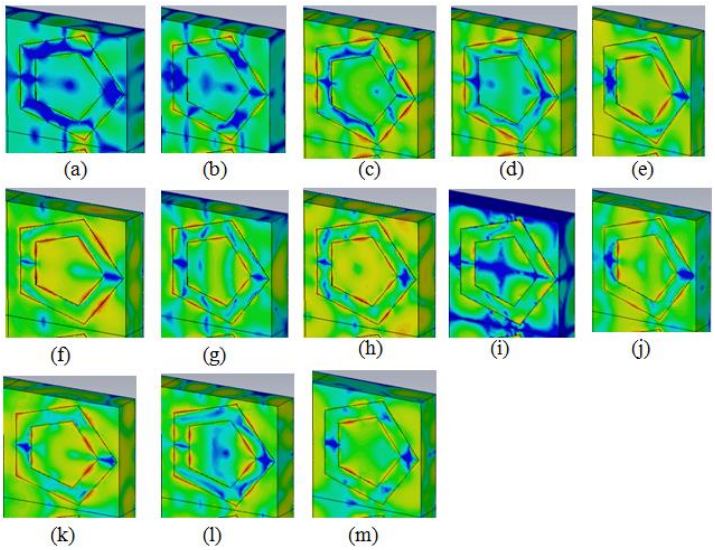

Fig. 5. Electric field distribution of thirteen-band absorber for the resonance frequencies of (a) 0.77 THz, (b) 0.78 THz, (c) 0.8 THz, (d) 0.81 THz, (e) 0.84 THz, (f) 0.85 THz, (g) 0.86 THz, (h) 0.87 THz, (i) 0.876 THz, (j) 0.88 THz, (k) 0.89 THz, (l) 0.9 THz, (m) 0.94 THz (color online)

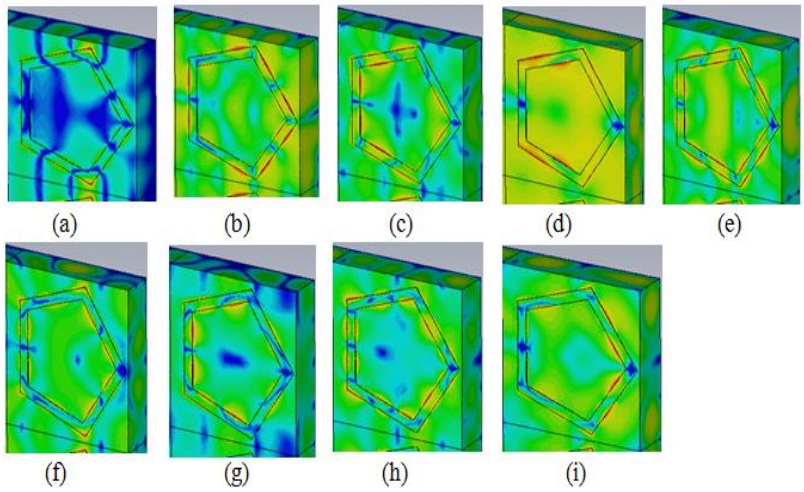

Fig. 6. Electric field distribution of nine-band absorber for the resonance frequencies of (a) 0.78 THz, (b) 0.79 THz, (c) 0.82 THz, (d) 0.83 THz, (e) 0.85 THz, (f) 0.86 THz, (g) 0.89 THz, (h) 0.92 THz, (i) 0.93 THz (color online)

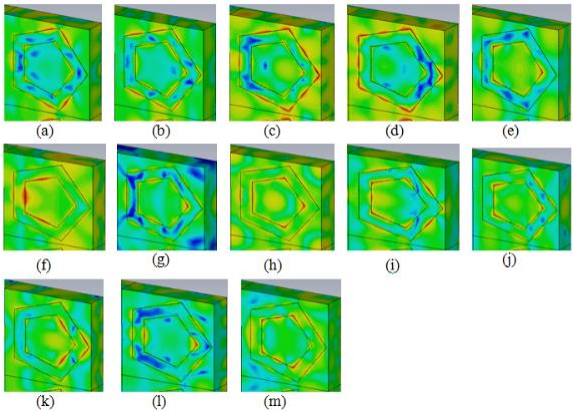

Fig. 7.Magnetic field distribution of thirteen-band absorber for the resonance frequencies of (a) 0.77 THz, (b) 0.78 THz, (c) 0.8 THz, (d) 0.81 THz, (e) 0.84 THz, (f) 0.85 THz, (g) 0.86 THz, (h) 0.87 THz, (i) 0.876 THz , (j) 0.88 THz, (k) 0.89 THz, (l) 0.9 THz, (m) 0.94 THz (color online)

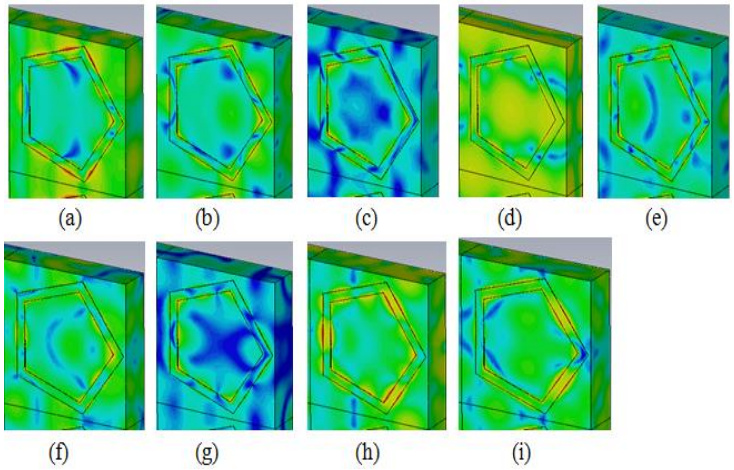

Fig. 8. Magnetic field distribution of nine-band absorber for the resonance frequencies of (a) 0.78 THz, (b) 0.79 THz, (c) 0.82 THz, (d) 0.83 THz, (e) 0.85 THz, (f) 0.86 THz, (g) 0.89 THz, (h) 0.92 THz, (i) 0.93 THz (color online)

THz the E-field is maximum at the surface of the dielectric and the outer bends of the pentagon resonator and the frequency of 0.82 THz the E-field is maximum at the surface of the dielectric and the inner bends of the pentagon resonator. When the frequency is 0.83 THz the E-field is maximum at the whole patch structure and surface of the dielectric. For the frequency of 0.85 THz, 0.86 THz, 0.89 THz, 0.92 THz and 0.93 THz the E-field is maximum at the inner and outer edges and bends of the pentagon resonator and the dielectric surface.

3.3. Magnetic field distributions (M - field)

The magnetic field distribution diagram for thirteen absorption bands is shown in Fig. 7. The magnetic field distribution diagram for these thirteen absorption bands is shown in Fig. 5. It can be observed from Fig. 7 (a), (b) (c) (d) that the absorption mode at 0.77 THz, 0.78 THz, 0.8 THz and 0.81 THz respectively, is obtained due to the field distribution near the outer edges of the pentagon resonator, which is caused by the slowing of charges near the edges and on the surface of the dielectric. When the frequency is 0.84 THz the M-field is maximum at the outer edges of the pentagon resonator and surface of the dielectric. For the frequency of 0.85 THz, 0.87 THz, 0.876 THz, 0.88 THz, 0.89 THz and 0.94 THz the M-field is maximum at the whole patch structure and surface of the dielectric. When the frequencies are 0.86 THz and 0.9 THz the M-field is maximum at inside of the resonator structure and the dielectric surface. The magnetic field distribution diagram for nine absorption bands is shown in Fig.8. For the frequency of 0.78 THz, 0.79 THz, 0.83 THz, 0.86 THz, 0.92 THz and 0.93 THz the M-field is maximum at the whole patch structure and surface of the dielectric. 0.82 THz, 0.89 THz and 0.85 THz the magnetic field is maximum at whole patch structure and some places in surface of the dielectric.

3.4. Parametric study

Parametric examination can be directed to research the size impact of components towards the working frequency. For all cases, copper metal is used as a ground plane to block the transmission waves. For the parametric analysis part, we discuss the effect of the inner radius of the pentagon r_2 on the absorption spectra. By changing r_2 from 0.12 mm to 0.22 mm the modes are drifted to lower frequency as shown in Fig.10. The absorption of all the modes depends upon the inner radius r_2 (0.12 mm, 0.14 mm, 0.18 mm, 0.22 mm) are clearly shown in graphs Fig.11 (a-d). Fig.2 (a-b) shows the 0.16 mm, 0.2 mm based MMA structure results. To conclude, from the above analysis, we are getting thirteen-/nine-bands only when r_1 value is 0.24 mm and r_2 value is 0.16 mm (thirteen-band), 0.2 (nine-band).

3.5. Sensing mechanism

The sensing nature of the structure is analysed by placing 0.001 mm analyte over the top layer structure which is shown in Fig.9. In order to increase the RI value from 1 to 2 the curves are shifted from the original position. Based on that we calculated the sensing amount. We label the thirteen resonance absorption peaks as modes *A* to *M*. In common, the *Q* (and the definition of the *Q* is the resonance frequency point divided by its Full Width Half Maximum (FWHM)) value is a significant pointer in judging the use of the resonance mode.

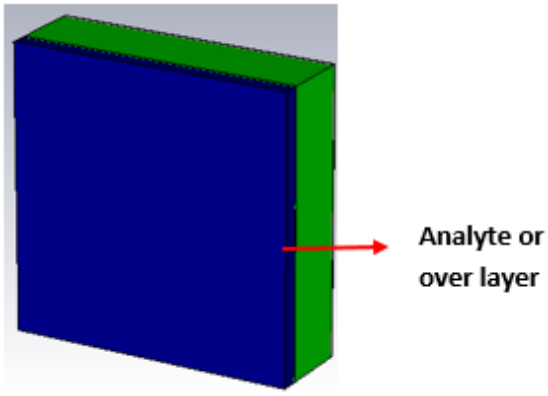

Fig. 9. Analyte over the top patch layer (color online)

It can openly reproduce whether the frequency mode can be used in sensing. Sensing performance is better when the *Q* value is higher [26]. Along with the explanation of the *Q* value, the *Q* value of the *F* mode frequency point can be up to 423, which is much larger than that of the other frequency points. For the detailed discussion of it, the Q, FOM, FWHM, sensitivity (*S*) with corresponding resonant frequencies are tabulated in Table 1. To examine whether the designed absorber can be included into sensor to monitor or detect the variation of the refractive index (RI) of environment, which are enclosed above the top patch resonator. The dependence of the absorption peak on the change of the RI of the over layer is shown in Fig.11. When the RI is changed from vacuum $n = 1$ to $n = 2$ in intervals of 0.2 For biological applications the refractive index of the bio molecules in RNA varies from 1.6 to 2 and in the DNA varies from 1.4 to 1.6 [34-35]. Actually, the refraction index sensitivity (*S*) is a sensitive factor to illustrate sensing mechanism of the resonance structure, and the sensitivity can be defined as $S = df/dn$, where *dn* is the change of the RI and *df* is the change of the resonance frequency [27, 28]. It can be seen that the *S* of the frequency points *A* to *D* are have 0.03 THz and the frequency points *G* to *I* and *M* have 0.02 THz. The sensitivity of the frequency points, *F*, *K* and *L* has 0.1 THz, 0.1 THz, 0.14 THz and 0.27 THz respectively. Compared with the *S* values of the frequency points *A-M*, the *S* enhancement factors for the frequency point *E*, *F*, *K* and *L* can be high. Besides the sensitivity, the FOM (figure of merit) is a more important factor to calculate the sensor quality and allows a straight comparison of sensing amount between different sensors [29]. The FOM is calculated by, $FOM = S/\text{FWHM}$. Based on the *S* values and the FWHM of the thirteen resonance modes, the FOMs of the frequency points *(A-M)* values are shown in Table 1. More importantly, the FOM and Q-factor of the frequency point *F* is much larger than previous works operated at the terahertz frequency range [30-33]. As a result of these outstanding qualities, the design of the thirteen-band absorber is promising in sensor-related fields. The fabrication method contains two main steps. The first step is to coat a copper metal over the polyimide substrate which will use the DC Magnetron sputtering unit model with the pressure level of 2×10^{-5} bar and the temperature level of 250^{0c}. Then laser micromachining process is used to ablate the material from the target material. After the fabrication mechanism, the ablated area in the material will be study by using optical images and scanning electron microscopic images. THz-TDS spectroscopy will be used to characterize the fabricated array structure for the terahertz frequency range. This work is compared with previous works which is shown in Table 2.

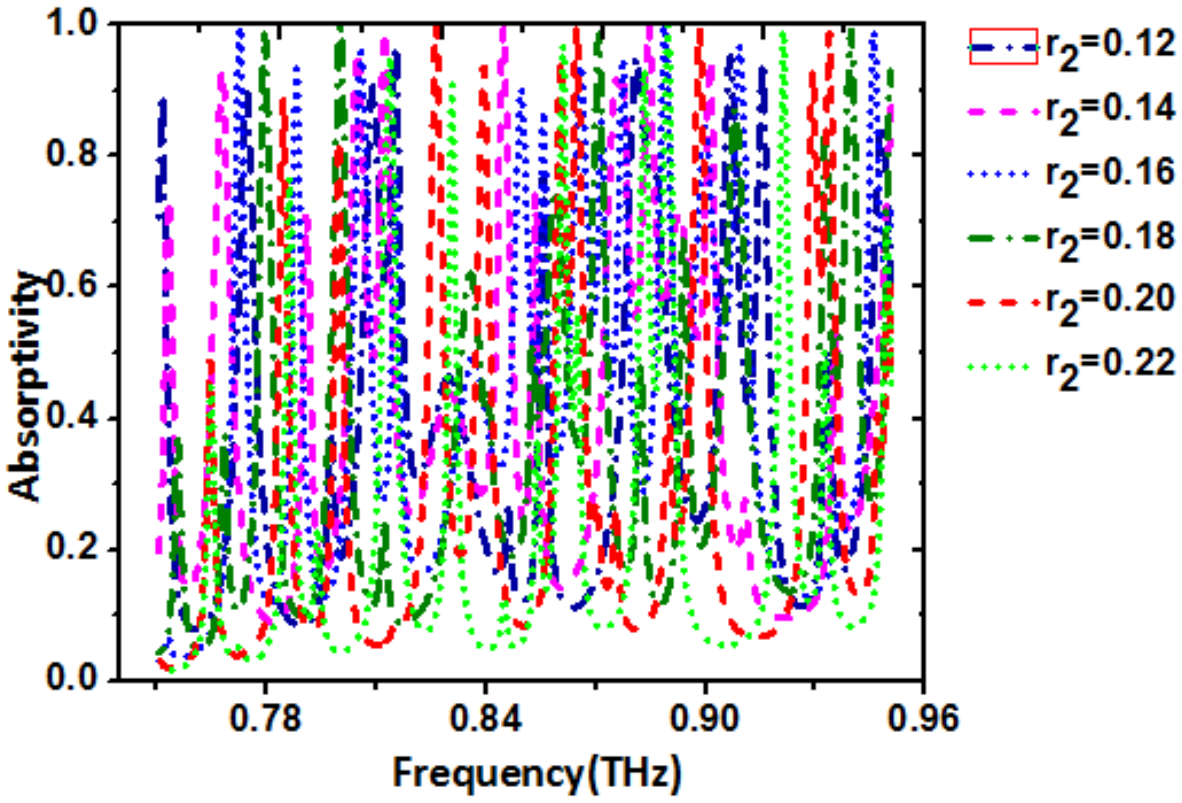

Fig.10. Variation in the absorption bands for the TE polarization with respect to r_2 (color online)

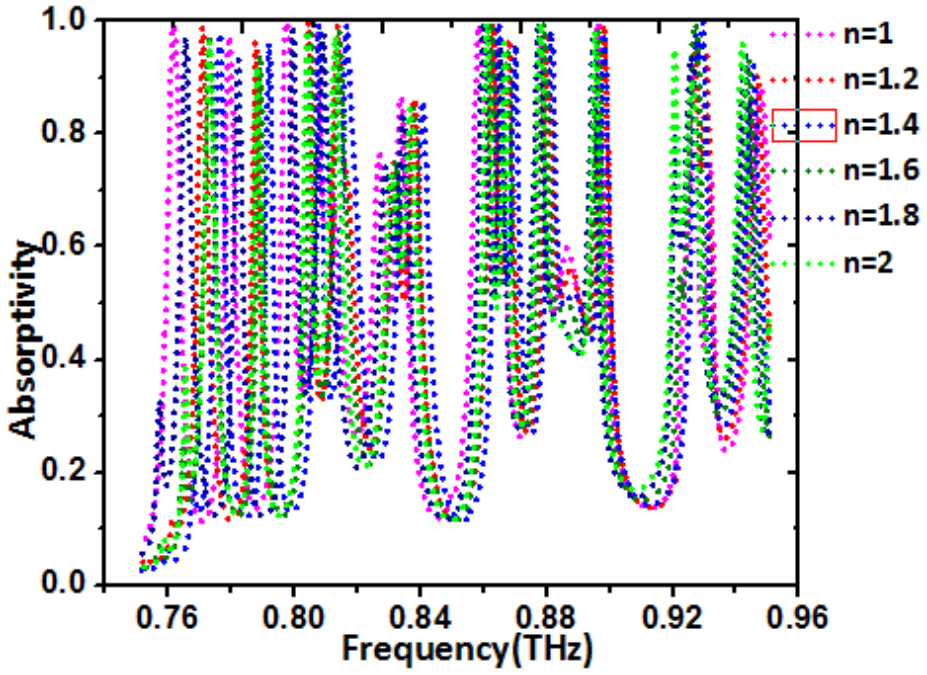

Fig. 11. Absorption of the MMA sensor at different analyte refractive indices (color online)

Table 1. Q-factor and FOM values for thirteen frequencies

Resonant Frequencies (THz)	Resonant mode points	FWHM	Q=Freq/FWHM	S=df/dn (THz/RIU)	FOM=S/FWHM
0.77	A	0.0032	240.625	0.037	11.5625
0.78	B	0.00311	250.80	0.0315	10.1286
0.8	C	0.00422	189.57	0.0315	7.464
0.81	D	0.00296	273.64	0.031	10.472
0.84	E	0.00644	130.43	0.1035	16.071
0.85	F	0.00201	**423**	0.1015	**50**
0.86	G	0.00324	265.43	0.02	5.55
0.87	H	0.00208	418.26	0.02	7.69
0.876	I	0.00298	293.95	0.02	5.53
0.88	J	0.0034	258.82	0.055	16.17
0.89	K	0.00389	228.79	0.14	35.98
0.9	L	0.01165	77.25	0.27	23.47
0.94	M	0.00703	133.71	0.0265	3.76

Table 2. Comparison of the proposed absorber structure with previous multi-band absorbers

Ref.	Frequency range	No. of bands	Materials	Polarization stability	Angle stability
[22]	(0.9-1.8) THz	1	Au, benzocyclobutane, Au	insensitive	insensitive
[21]	(0-3.5) THz	2	Au, Si, Au	insensitive	insensitive
[20]	(0-1.5) THz	3	Au, Polyimide, Au	insensitive	insensitive
[23]	(1-7) GHz	4	Cu, FR_4, Cu	insensitive	insensitive
[19]	(0.5-2.5) THz	4	Au, Polyimide, Au	No analysis	No analysis
[18]	(0.5-3.5) THz	5	Au, Polyimide, Au	insensitive	No analysis
[17]	(0-5) THz	6	Si, Cu, Polyimide, Cu	No analysis	No analysis

Ref.	Frequency range	No. of bands	Materials	Polarization stability	Angle stability
[16]	(4-12) GHz	7	Cu, FR_4, Cu	insensitive	insensitive
[15]	(0.5-3.5) THz	8	Au, GaAs, Au	insensitive	Both angle sensitive as well as angle insensitive.
This work	**(0.76-0.96)** THz	13	Cu, Polyimide, Cu	Both polarization-sensitive as well as polarization-insensitive	Both angle sensitive as well as angle insensitive.

4. Conclusion

In conclusion, we present a novel and simpler design of terahertz metamaterial absorber and the proposed structure consists of copper as a ground plane and polyimide dielectric layer is placed in between the ground panel and top radiating patch. The device exhibits both, thirteen-band absorption response at the frequency of 0.77 THz, 0.78 THz, 0.8 THz, 0.81 THz, 0.84 THz, 0.85 THz, 0.86 THz, 0.87 THz, 0.876 THz, 0.88 THz, 0.89 THz, 0.9 THz and 0.94 THz and nine-band absorption performance at the frequency of 0.78 THz, 0.79 THz, 0.82 THz, 0.83 THz, 0.85 THz, 0.86 THz, 0.89 THz, 0.92 THz and 0.93 THz. This is achieved by adjusting the single top patch geometrical parameter. This MMA can provide thirteen-/nine-band high-level absorption performance in a single planar structure for the first time in terahertz range. The unique feature of the design is that it offers both polarization-sensitive-/insensitive and angle-insensitive-/sensitive absorption characteristics depending on the frequency of operation, when the angle of polarization and incidence of the electromagnetic wave is varied. Particularly, the design gives a significant ability to shift the resonance frequencies by changing different geometric parameters. Thus, our design will have potential application in material detection and biological sensing.

References

[1] M. Tonouchi, Nat. Photonics **1**, 97 (2007).
[2] D. R. Smith, W. J. Padilla, D. C. Vier, S. C. Nemat-Nasser, S. Schultz, Phys Rev Lett. **84**, 4184 (2000).
[3] V. G. Veselago, Sov. Phys. Uspekhi **10**(4), 509 (1968).
[4] Hiroki Wakatsuchi, John Paul, Christos Christopoulos, IEEE Trans. Antennas Propag. **60**, 5743 (2012).
[5] G. Rosenblatt, M. Orenstein, 2016 Progress in Electromagnetic Research Symposium (PIERS), Shanghai, 4946 (2016).
[6] Y. J. Yoo, H. Y. Zheng, Y. J. Kim, J. Y. Rhee, J. H. Kang, K. W. Kim, Y. P. Lee, Journal Applied Physics Letters **105**, 041902 (2014).
[7] A. T. Devapriya, S. Robinson, J. Microw. Optoelectron. Electromagn. Appl. **18**, 377 (2019).
[8] Jianjun Liu, Zhi Hong. Opt. Commun. **1**, 598 (2018).
[9] Patrick Rufangura, Cumali Sabah, Vacuum **120**, 68 (2015).
[10] M. M. Gajibo, M. K. A. Rahim, N. A. Murad, O. Ayop, H. A. Majid, 2017 IEEE Asia Pacific Microwave Conference (APMC), Kuala Lumpar, 509 (2017).
[11] Fei Yan, Qi Li, Hao Tian, Zewen Wang, Li Li, J. Phys. D Appl. Phys. **53**, 235103 (2020).
[12] M. L. Hakim, T. Alam, A. F. Almutairi, M. F. Mansor, M. T. Islam, Sci. Rep. **11**(1), 1 (2021).
[13] Ben-Xin Wang, Yuanhao He, Pengcheng Lou, Wenhui Xing, Nanoscale Advances **2**, 763 (2020).
[14] N. I. Landy, S. Sajuyigbe, J. J. Mock, D. R. Smith, W. J. Padilla, Phys. Rev. Lett. **100**, 207402 (2008).
[15] V. K. Verma, S. K. Mishra, K. K. Kaushal, V. Lekshmi, S. Sudhakar, S. K. Mishra, B. Appasani, N. Gupta, Plasmonics **15,** 75 (2020).
[16] Y. Cheng, Y. Zou, H. Luo, F. Chen, X. J. Mao, Electron. Mater. **48**, 3939 (2019).
[17] D. Hu, H. Wang, Q. Zhu, IEEE Photonics J. **8**, 1 (2016).
[18] G. Z. Wang, B. X. Wang, J Lightwave Technol. **33**, 5151 (2015).
[19] B. Wang, G. Wang, IEEE Photonics J. **8**, 1 (2016).
[20] A. Shoieb, J. Nourinia, C. Ghobadi, M. Karamirad, B. Mohammadi, 5th Conference on Knowledge Based Engineering and Innovation (KBEI), Tehran, Iran, 042 (2019).
[21] B. X. Wang, G. Z. Wang, L. L. Wang, Plasmonics **11**, 523 (2016).
[22] M. D. Astorino, F. Frezza, N. Tedeschi, J. Appl. Phys. **121**, 063103 (2017).
[23] M. Edries, H. A. Mohamed, S. S. Hekal, M. A. El-Morsy, H. A. Mansour, IEEE Access **8**, 143723 (2020).
[24] A. Mohanty, O. P. Acharya, B. Appasani, S. K. Mohapatra, Photonics Nanostruct. **32**, 74 (2018).
[25] Devkinandan Chaurasiya, Saptarshi Ghosh, Somak Bhattacharyya, Anamiya, Srivastava Bhattacharya, Vaibhav Kumar, IET Microwaves, Antennas & Propagation. **10**, 94 (2016).
[26] Q. Xie, G. Dong, B. Wang, W. Huang, Nanoscale Res. Lett. **13**, 137 (2018).
[27] C. Sabah, B. Mulla, H. Altan, L. Ozyuzer, Pramana – J. Phys. **91**, 17 (2018).
[28] L. Cong, S. Tan, R. Yahiaoui, F. Yan, W. Zhang, R. Singh, Appl. Phys. Lett. **106**, 031107 (2015).
[29] X. Yu, L. Shi, D. Han, J. Zi, P. V. Braun, Adv. Funct. Mater. **20**, 1910 (2010).

[30] Tao Chen, Runyu Zhao, Ben-Xin Wang, Applied Sciences **9**, 1410 (2019).
[31] R. Singh, W. Cao, I. Al-Naib, L. Cong, W. Withayachumnankul, W. Zhang, Appl. Phys. Lett. **105**, 171101 (2014).
[32] I. Al-Naib, IEEE Journal of Selected Topics in Quantum Electronics **23**(4), 1 (2017).
[33] Q. Xie, G. X. Dong, B. X. Wang, W. Q. Huang, Nanos. Res. Lett. **13**, 294 (2018).
[34] B. M. Fischer, M. Walther, P. U. Jepsen, J. Biomed.Phys. Eng. **47**, 3807 (2002).
[35] M. Fischer, Opt. Express **13**, 5205 (2005).

* Corresponding author: elakkiyaa@saveetha.ac.in